Bifurcations in droplet collisions

A. Dubey,[1] K. Gustavsson ®,[1] G. P. Bewley,[2] and B. Mehlig ®[1]

[1]*Department of Physics, Gothenburg University, 41296 Gothenburg, Sweden*
[2]*Sibley School of Mechanical and Aerospace Engineering, Cornell University, Ithaca, New York 14853, USA*

Saffman and Turner [P. G. Saffman and J. S. Turner, J. Fluid Mech. **1**, 16 (1956)] argued that the collision rate for droplets in turbulence increases as the turbulent strain rate increases. However, the numerical simulations of Dhanasekaran *et al.* [J. Dhanasekaran *et al.*, J. Fluid Mech. **910**, A10 (2021)] in a steady straining flow showed that the Saffman-Turner model is oversimplified because it neglects droplet-droplet interactions. These result in a complex dependence of the collision rate on the strain rate and on the differential settling speed. Here we show that this dependence is explained by a sequence of bifurcations in the collision dynamics. We compute the bifurcation diagram when strain is aligned with gravity and show that it yields important insights into the collision dynamics. First, the steady-state collision rate remains nonzero in the limit Kn → 0, contrary to the common assumption that the collision rate tends to zero in this limit (Kn is a nondimensional measure of the mean free path of air). Second, the nonmonotonic dependence of the collision rate on the differential settling speed is explained by a grazing bifurcation. Third, the bifurcation analysis explains why so-called closed trajectories appear and disappear. Fourth, our analysis predicts strong spatial clustering near certain saddle points, where the effects of strain and differential settling cancel.

I. INTRODUCTION

Turbulent aerosols are suspensions of particles or droplets in a turbulent flow. Common examples are droplets or ice crystals in atmospheric clouds [1] and dust particles in circumstellar accretion disks [2]. The physical properties of such systems are determined by collisions between the particles [3,4]. In clouds, turbulent strains bring droplets into close contact [5]. Apart from this mechanism, their collision dynamics is influenced by gravity, hydrodynamic forces, and direct electrostatic interactions if the droplets are charged [6]. Fluid-mediated hydrodynamic interactions tend to bend the paths of two approaching droplets around each other [7], potentially preventing collision. However, when the droplets are very close, i.e., when their interfacial separation is smaller than the mean free path of air, the hydrodynamic approximation breaks down, reducing the hydrodynamic repulsion of approaching droplets [8]. Another factor that affects collision rates is particle inertia, which allows the droplets to detach from the flow, increasing the collision rate [9]. Larger droplets may accelerate the surrounding fluid significantly, so convective fluid inertia must be taken into account for similar-size droplets [10]. In other words, the collision dynamics of droplets in turbulence is quite complex, and though it has been studied for more than 50 years, it is not
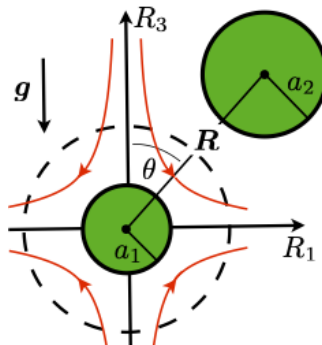
FIG. 1. Two droplets settling in a straining flow (thin red lines), shown in the rest frame of the smaller droplet, with radius $a_1 < a_2$. The compressive direction of the strain is aligned with gravity $\boldsymbol{g}$. Since the system has rotation symmetry about the R_3 axis, it suffices to analyze the dynamics in the R_1-R_3 plane.

known how to parametrize the collision rate in terms of the nondimensional parameters: the Stokes number St (particle inertia), the nondimensional differential settling speed Q (gravitational settling), turbulence intensity (strength of the turbulent strains), Reynolds and Strouhal numbers (fluid inertia), the Coulomb number (electrostatic interactions), the Knudsen number Kn (breakdown of the hydrodynamic approximation at distances smaller than the mean free path of air), and the ratio of droplet radii.

Saffman and Turner [5] computed the effect of turbulent strain on the collision rate, assuming that the droplets follow the flow, neglecting all other interactions between them. They found that the collision rate for droplets of radii a_1 and a_2 increases with strain s as $\mathscr{R}_s \sim n_0(a_1 + a_2)^3 s$, where n_0 is the particle-number density. They compared with the collision rate of small spherical droplets settling under gravity in a quiescent fluid, $\mathscr{R}_g \sim n_0 v_s (a_1 + a_2)^2$, where $v_s = \frac{2\rho_p}{9\rho_f}(a_2^2 - a_1^2)g/\nu$ is the differential settling speed with viscosity ν, gravitational acceleration g, and ratio of droplet and air mass densities $\rho_p/\rho_f \gg 1$. Their main conclusions are that turbulence facilitates collisions between droplets of similar sizes and that the collision rate increases as the turbulent strain s increases. However, Fig. 10 of Ref. [11] indicates that this picture may be oversimplified. Dhanasekaran *et al.* [11] computed the collision dynamics of small spheres settling in a steady straining flow, taking into account hydrodynamic interactions and the breakdown of the hydrodynamic approximation at small separations. Their model neglects effects of particle and fluid inertia, electrostatic interactions, van-der Waals forces, and unsteady turbulent fluctuations. Their numerical results show that the interactions reduce the collision rate and that it depends sensitively on the nondimensional differential settling speed Q, a measure of the relative strength of strain and gravity.

Here we show that the observed dependence of the collision rate upon Q reflects qualitative changes—bifurcations—in the collision dynamics as Q is varied. We analyzed the bifurcations for a specific example [11]: two droplets of different sizes settling in a steady straining flow. We chose a straining flow aligned with the direction of gravity (Fig. 1). We found the equilibria of the collision dynamics and we determined how they appear, disappear, and how their stabilities and invariant manifolds change as the parameter Q is varied.

The bifurcation analysis allows the following conclusions. First, for a certain range of Q values, the steady-state collision rate becomes independent of Kn for small Knudsen numbers, contrary to the common assumption that droplets cannot collide in this limit [1,12–14]. Second, a global grazing bifurcation (called ⓐ below) causes a sensitive dependence of the collision rate upon Q. Third, our bifurcation analysis allows us to understand the significance of so-called closed trajectories that appear and disappear as Q is varied. These are trajectories that start and end on the collision sphere [11,15–17]. Fourth, we find strong spatial clustering near certain saddle points, on their unstable

invariant manifolds. In our model this leads to a divergent pair correlation function at separations of the order of several droplet radii.

Our main conclusions rely on the fact that the collision dynamics has a boundary at $R = a_1 + a_2$. The global grazing bifurcation occurs when an invariant manifold collides with this boundary [18,19]. Grazing bifurcations are usually discussed for piecewise smooth dynamical systems [19–21]. In such systems boundaries occur between the smooth parts. In our case, however, the radial derivative of the relative droplet velocity diverges at the boundary $R \to a_1 + a_2$, so our system is not piecewise smooth. This is the origin of the sensitive dependence of the collision rate upon Q mentioned above.

II. MODEL

We begin with the definition of the nondimensional parameters St and Q. The Stokes number is defined as $\mathrm{St} = s\tau_p$ with strain rate s and particle response time $\tau_p = (2\rho_p/9\rho_f)(\overline{a}^2/\nu)$, where $\overline{a} = (a_1 + a_2)/2$ is the mean particle radius. The effect of gravity is parametrized by the nondimensional differential settling speed $Q = v_s/\overline{a}s$. Here we consider droplets small enough so that we can take the limit $\mathrm{St} \to 0$. At the same time we assume that Q remains finite. In this overdamped limit, the relative dynamics is just given by $\dot{\boldsymbol{R}} = \boldsymbol{V}(\boldsymbol{R})$, where $\boldsymbol{R} = \boldsymbol{x}^{(2)} - \boldsymbol{x}^{(1)}$ is the spatial separation between two particle centres and $\boldsymbol{V} = \boldsymbol{v}^{(2)} - \boldsymbol{v}^{(1)}$ is their relative velocity. This limit neglects singularities and multivalued particle velocities in the inertial collision dynamics due to caustics [22–24]. The probability of observing two droplets at separation $\boldsymbol{R}$ is given by the continuity equation

$$\frac{\partial P(\boldsymbol{R}, t)}{\partial t} + \nabla \cdot [\boldsymbol{V}(\boldsymbol{R})P(\boldsymbol{R}, t)] = 0, \tag{1}$$

with the boundary condition $P(\boldsymbol{R}, t) \to 1$ as $R \to \infty$. This boundary condition reflects the uniform spatial distribution at large separations of small droplets in an incompressible flow. The collision rate is given by [25]

$$\mathscr{R}_t = -\lim_{R \to a_1 + a_2} n_0 \int d\Omega \, V_R(\boldsymbol{R}) P(\boldsymbol{R}, t) \Theta(-V_R(\boldsymbol{R})), \tag{2}$$

where $V_R = \boldsymbol{V} \cdot \hat{\boldsymbol{R}}$ is the radial relative velocity, $R = |\boldsymbol{R}|$ is the center-of-mass distance between the droplets, Ω is the solid angle, and Θ is the Heaviside function.

Following Ref. [11], we consider a steady straining flow with velocity $\boldsymbol{u}(\boldsymbol{x}) = \frac{1}{2}(sx_1\hat{\mathbf{e}}_1 + sx_2\hat{\mathbf{e}}_2 - 2sx_3\hat{\mathbf{e}}_3)$, where $\hat{\mathbf{e}}_i$ denotes the unit vector in direction R_i (Fig. 1). The strain-rate matrix $\mathbb{S}$ is diagonal with entries $S_{11} = s/2$, $S_{22} = s/2$, and $S_{33} = -s$. We assume that the compressive axis of the strain is aligned with the gravitational acceleration (Fig. 1).

In the overdamped limit, the relative velocities $\boldsymbol{V}(\boldsymbol{R})$ are computed using the hydrodynamic mobility tensor that relates particle velocities to the given external forces in a linear flow [7]. The elements of this tensor depend on the particle radii a_1 and a_2 and on the particle separation $\boldsymbol{R}$. In nondimensional variables ($\boldsymbol{R} \to \boldsymbol{R}/\overline{a}$ and $t \to ts$) the equations of motion read [11]

$$\dot{R}_i = V_i,$$

$$V_i = S_{ij}R_j - \left[A\frac{R_iR_k}{R^2} + B\left(\delta_{ik} - \frac{R_iR_k}{R^2}\right)\right]S_{kl}R_l - \left[L\frac{R_iR_k}{R^2} + M\left(\delta_{ik} - \frac{R_iR_k}{R^2}\right)\right]Q\,\delta_{k3}, \tag{3}$$

where summation over repeated indices is implied. Here A, B, L, and M are mobility functions, formed using elements of the mobility tensor mentioned above. These mobility functions depend only upon the droplet separations and their radius ratio. The mobility functions are not known in closed form. To evaluate A, B, L, and M, we use series expansions in a/R derived in Refs. [26–28]. In this hydrodynamic approximation, the radial mobilities $1 - A$ and L decay linearly to zero as the interfacial separation between the droplets vanishes. However, when the interfacial separation between the droplets becomes comparable to the mean free path of air ℓ, the hydrodynamic approximation breaks down. This gives rise to nonhydrodynamic effects, parametrized by the

Knudsen number $\text{Kn} = \ell/\overline{a}$. Sundararajakumar and Koch [8] derived how these effects change the functional form of the mobility functions on close approach. Dhanasekaran *et al.* [11] showed how to match the radial noncontinuum mobilities A and L to the series expansions of their hydrodynamic counterparts. We followed this approach, and like Ref. [11] we did not account for Kn corrections to the tangential mobilities B and M. While noncontinuum effects may change how the mobilities approach their values upon contact [29], it is expected that this change has a small effect on the collision dynamics [11], at least when the droplet radii are not too different.

There are two reasons why the collision dynamics (3) is not smooth. First, the mobility functions are nonsmooth at $R = 2$. The radial mobilities decay to zero as $(\log\log\frac{\text{Kn}}{R-2})^{-1}$ as $R \to 2$ and the radial derivative of this expression diverges in this limit. This means that the dynamics is not unique once it reaches $R = 2$. The tangential mobilities behave as $(\log\frac{1}{R-2})^{-1}$ near $R = 2$. The nonsmoothness of the mobilities means that bifurcations at $R = 2$ need not have the normal forms known for smooth dynamical systems [30,31]. Second, we assume that the droplets coalesce upon collision, so the dynamics arrests on the collision sphere, at $R = 2$. The collision sphere therefore acts as a boundary, allowing global grazing bifurcations [18,19] to occur.

III. RESULTS

A. Phase portraits

Figure 2 shows phase portraits of the collision dynamics. We plotted the droplet paths in the R_1-R_3 plane, in the rest frame of the smaller droplet. It suffices to consider the dynamics in the R_1-R_3 plane because the system has rotational symmetry about the R_3 axis when the compressive axis of strain is aligned with gravity. Figure 2(a) shows the phase portrait for $\text{Kn} = 10^{-3}$ and a small value of the nondimensional settling velocity ($Q = 0.9$) where strain dominates and gravitational settling is of secondary importance. There are four fixed points, labeled I, II, III, and II′. The phase portrait is symmetric under the reflection $R_1 \to -R_1$, and we label the symmetric counterpart of a fixed point by a prime. The phase portrait shown in Fig. 2(a) is very similar to that at $Q = 0$, just slightly distorted. At $Q = 0$, the relative-velocity field $\boldsymbol{V}(\boldsymbol{R})$ is symmetric under reflections $R_3 \to -R_3$ and $R_1 \to -R_1$. Therefore, $\boldsymbol{V}$ must be parallel to $\hat{\mathbf{e}}_3$ for $R_1 = 0$, and $\boldsymbol{V} \propto \hat{\mathbf{e}}_1$ for $R_3 = 0$. Using that the radial velocity vanishes at $R = 2$, we obtain

$$\begin{bmatrix} 2 \\ 0 \end{bmatrix} \text{ (I)}, \quad \begin{bmatrix} 2 \\ \frac{\pi}{2} \end{bmatrix} \text{ (II)}, \quad \begin{bmatrix} 2 \\ \pi \end{bmatrix} \text{ (III)}, \quad \begin{bmatrix} 2 \\ \frac{3\pi}{2} \end{bmatrix} \text{ (II′)} \tag{4}$$

for the locations $[R^*, \theta^*]$ of the four fixed points at $Q = 0$. Here $R \equiv |\boldsymbol{R}|$ and θ is the polar angle measured from the positive R_3 axis (Fig. 1). For nonzero values of Q, symmetry implies that θ^* remains at 0 for I and at π for III. The precise locations of II and II′ on the collision sphere are given in Appendix A. The velocity field cannot be linearized on the collision sphere. Nevertheless, the flow near these fixed points resembles that near a saddle, with stable and unstable manifolds. Saddles I and III have stable manifolds on the R_3 axis, while II and II′ have unstable manifolds on the R_1 axis. In addition, the fixed points are connected by manifolds on the collision sphere (not shown). Figure 2(a) indicates that droplets approach along the stable manifolds of saddles I and III and escape along the unstable manifolds of II and II′. The trajectory separating colliding trajectories from noncolliding ones is a grazing trajectory: It is tangential to the collision sphere at the point where it touches the collision sphere (marked by a circle).

Figure 2(b) corresponds to $Q = 6.20$ and $\text{Kn} = 10^{-3}$. This phase portrait is qualitatively different from that in Fig. 2(a). There are additional fixed points, suggesting that bifurcations occurred. The new fixed points are a stable node N and a saddle point IV as well as their symmetric counterparts. Note that the node N is very close to the saddle point II; they cannot be distinguished in the figure. We see that a grazing trajectory determines collision outcomes for paths approaching from $R_3 = +\infty$. However, for paths approaching from $R_3 = -\infty$, the separatrix between colliding and noncolliding trajectories is formed by stable manifolds of the saddle points IV and IV′. One stable
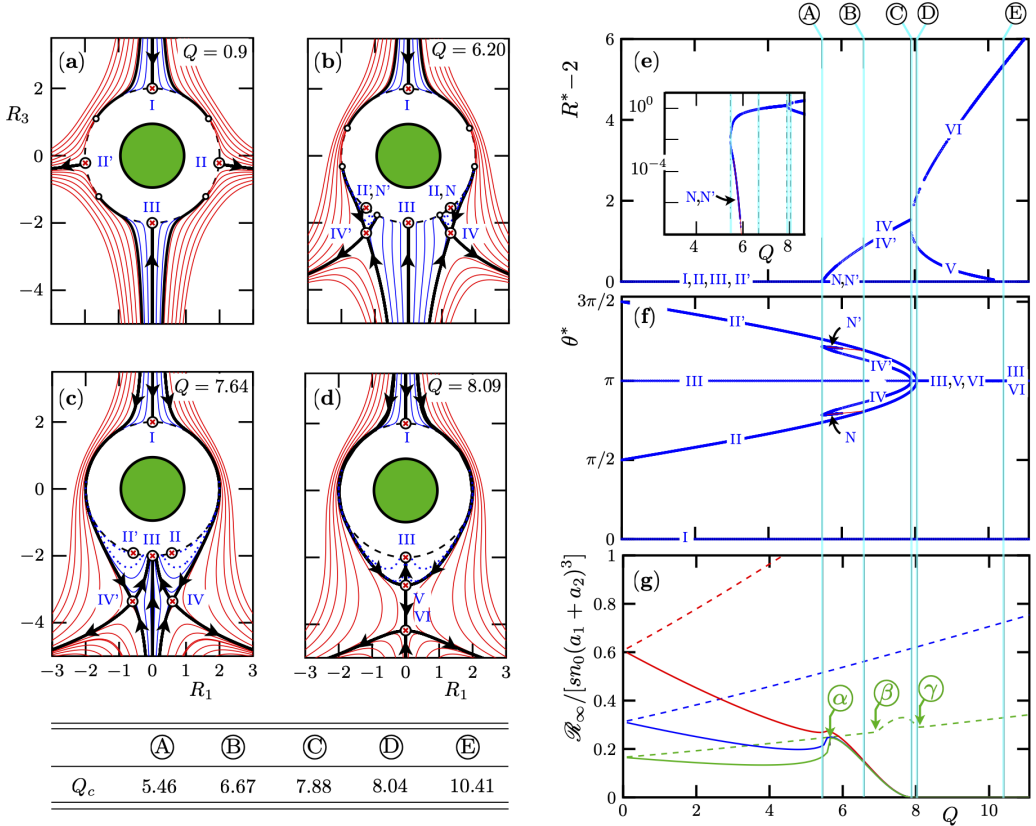
FIG. 2. (a)–(d) Phase portraits of the collision dynamics for different values of the nondimensional differential settling speed Q. Trajectories lead to collision (blue), no collision (red), invariant manifolds and grazing trajectories (black solid), and the collision sphere (dashed). In (b)–(d) closed trajectories that begin and end on the collision sphere are plotted as blue dotted lines. Encircled red crosses denote fixed points. Small white circles on the collision sphere denote end points of grazing trajectories or invariant manifolds. (a) $Q = 0.9$, $a_1/a_2 = 0.9$, and Kn $= 10^{-3}$. (b) $Q = 6.20$. (c) $Q = 7.64$. (d) $Q = 8.09$. In (c) and (d) the stable manifolds of IV and IV$'$ and of V, respectively, coming from $R_3 = \infty$ are close to but do not touch the collision sphere. (e) and (f) Bifurcation diagrams for $a_1/a_2 = 0.9$ and Kn $= 10^{-3}$, showing the locations $[R^* - 2, \theta^*]$ of the fixed points I–VI, N, and their symmetric counterparts (primed). Blue curves correspond to numerical data and red lines in (f) to Eq. (B8). The inset in (e) shows the same data, but with a logarithmic y axis. The table lists the locations of the bifurcations Ⓐ–Ⓔ, also shown as vertical lines in the panels on the right. (g) Steady-state collision rate $\mathscr{R}_\infty$ as a function of Q for $a_1/a_2 = 0.9$ and Kn $= 10^{-1}$ (red), 10^{-2} (blue), and 10^{-3} (green). Dashed lines show the collision rate due to droplets approaching from $R_3 = +\infty$, while solid lines correspond to droplets approaching from $R_3 = -\infty$. Also shown are the locations of the three grazing bifurcations α–γ for Kn $= 10^{-3}$.

and one unstable manifold of the saddle IV intersect the collision sphere. The same is true for IV$'$. Between these stable and unstable invariant manifolds, there are closed trajectories that start and end on the collision sphere [11,15–17], shown as blue dotted lines.

Figure 2(c) shows the collision dynamics for $Q = 7.64$ and Kn $= 10^{-3}$. The nodes disappeared and the stable manifold of the saddle IV which previously intersected the collision sphere now extends to $R_3 \to +\infty$. It does not touch the collision sphere. This is difficult to see in Fig. 2(c), but important because it allows trajectories approaching from above to hit the collision sphere from below. The same conclusion holds for the invariant manifolds of IV$'$. In other words, the separatrices

between colliding and noncolliding trajectories from above are no longer grazing trajectories, but the stable manifolds of IV and IV'. As in Fig. 2(b), there are closed trajectories in the small regions delineated by the stable and unstable manifolds of IV and IV' (shown as blue dotted lines).

Figure 2(d) corresponds to $Q = 8.09$ and Kn $= 10^{-3}$. We see that the saddle IV and its symmetric counterpart IV' collided, giving rise to two new saddles V and VI. Now the collision sphere is entirely shielded from below by the unstable manifolds of VI. The stable manifolds of V extend to $R_3 \to +\infty$ without touching the collision sphere. So again, some trajectories coming from $R_3 = \infty$ can collide from below. Finally, we see that the fixed points II and II' merged with III, which turned into a stable node.

In summary, the phase portraits in Fig. 2 are qualitatively different and we expect that the qualitative changes to the fixed points and their manifolds affect how the collision rate depends on Q and upon the Knudsen number Kn. To explain these dependences, we must first locate and characterize the bifurcations of the collision dynamics.

B. Bifurcations

The dynamical system (3) exhibits three different types of bifurcations when the parameters Q and Kn are varied. First, there are bifurcations of equilibria (labeled Ⓐ–Ⓔ below), where the number or types of equilibria change. Those bifurcations that occur at $R > 2$ are smooth; they must have the standard normal forms of smooth dynamical systems [30,31]. However, bifurcations at $R = 2$ need not be smooth, because the radial derivatives of the mobilities diverge as $R \to 2$, as mentioned above. Third, grazing bifurcations (labeled ⓐ–ⓖ below) are global bifurcations, where an invariant manifold, such as a separatrix, touches the collision sphere.

We begin by discussing the bifurcations of equilibria. Figures 2(e) and 2(f) show how their equilibrium locations $[R^*, \theta^*]$ change as Q is varied. The first bifurcation Ⓐ occurs at $Q_c = 5.46$. It is a saddle-node bifurcation where the saddle IV and the node N are created, as well as their symmetric counterparts IV' and N'. For Kn $= 10^{-3}$, this occurs at $R^* - 2 \approx 0.011$, quite close to the collision sphere. Nevertheless, since the dynamical system is smooth for $R > 2$, this is a standard smooth bifurcation. The location of the node is most clearly seen in the logarithmic scale of the inset in Fig. 2(e).

The next bifurcation Ⓑ is at $Q_c = 6.67$ where the nodes N and N' collide with the saddles II and II' on the collision sphere, and II and II' change from saddles to stable nodes. This bifurcation cannot occur in smooth dynamical systems, because in the absence of boundaries one can show that the sum of Poincaré indices of the fixed points participating in a bifurcation does not change [30]. We note that the Poincaré-index argument is readily extended to systems with boundaries: Enclose the fixed points II and N by a curve that starts and ends on the collision sphere, infinitesimally close to II. Since the saddle II changes into a node, the angle of rotation of the velocity field along this curve is conserved before and after bifurcation Ⓑ.

Numerical integration becomes difficult as N and N' approach the collision sphere. We therefore sought an asymptotic approximation describing how the location R^* of the nodes approach the collision sphere as Q tends to the bifurcation value $Q_c^{Ⓑ}$. We found

$$R^* \sim 2 + \exp[-20.49/(Q_c^{Ⓑ} - Q)] \tag{5}$$

for $Q < Q_c^{Ⓑ}$. Details of the derivation are given in Appendix B, which also contains a more accurate albeit more complicated expression [Eq. (B8)], plotted in Figs. 2(e) and 2(f) as red lines. The nonanalytic dependence on the parameter Q in Eq. (5) is a result of the divergence of the radial derivatives of the tangential mobility. In smooth systems, by contrast, bifurcation locations depend algebraically on $Q_c^{Ⓑ} - Q$ [30]. Equation (5) implies that $R^* - 2$ is almost zero long before Q has reached its bifurcation value $Q_c^{Ⓑ}$.

Bifurcation Ⓒ happens at $Q = 7.88$, where the saddles IV and IV' collide to form two new saddles V and VI. Since this bifurcation occurs at $R^* > 2$, it is a smooth bifurcation. At the bifurcation, two stable and two unstable manifolds of fixed points IV and IV' merge into a stable and

an unstable one. Both are oriented along $\hat{\mathbf{e}}_3$. The fixed point therefore has six invariant manifolds at the bifurcation: three stable and three unstable ones. After the bifurcation, the saddle points split along $\hat{\mathbf{e}}_3$, connected by a new heteroclinic trajectory.

At $Q = 8.04$, the fixed points II and II$'$ collide with III in a supercritical pitchfork bifurcation Ⓓ (see Appendix B), leaving behind only III, which turned from a saddle point to a stable node. This bifurcation occurs at $R = 2$, but it is nevertheless smooth. The reason is that the fixed points move along the collision sphere and the corresponding one-dimensional dynamical system is smooth. The nonsmooth behavior of the tangential mobilities does not qualitatively alter the bifurcation.

The last bifurcation of an equilibrium, Ⓔ, occurs at $Q_c = 10.41$, where the saddle point V collides with the node III on the collision sphere, which turns into a saddle point. This bifurcation cannot occur in smooth systems, where a saddle-node collision cannot result in a single saddle, as explained above. Note that the results shown in Figs. 2(e) and 2(f) are independent of the Knudsen number. The locations of the fixed points I, II, II$'$, and III depend only on tangential mobilities which do not depend upon Kn in the model considered here. The other fixed points depend upon the radial mobilities only through the combination $L/(1 - A)$, which is independent of the Knudsen number, as explained in Appendix B.

In addition to these bifurcations of equilibria, there are three grazing bifurcations, labeled with greek letters. Their locations are not shown in Figs. 2(e) and 2(f) because they are global bifurcations not described by changes in equilibria. For Kn $= 10^{-3}$, the grazing bifurcation ⓐ occurs at $Q_c = 5.67$, larger than but quite close to $Q_c^{Ⓐ}$. At this bifurcation, the unstable manifolds of the saddles IV and IV$'$ approaching the collision sphere end up intersecting it. The points of intersection are shown as circles in Fig. 2(b).

The grazing bifurcation ⓑ occurs at $Q_c^{ⓑ} = 7.6$ for Kn $= 10^{-3}$, when the stable manifolds of IV and IV$'$ approaching from $R_3 = \infty$ graze the collision sphere, allowing paths from above to hit the collision sphere from below for $Q > Q_c^{ⓑ}$. A final grazing bifurcation ⓒ occurs at $Q_c^{ⓒ} = 8.1$, where stable manifolds of the saddle V begin to graze the collision sphere, preventing trajectories approaching from above from colliding from below.

The locations of the grazing bifurcations depend on the Knudsen number. As Kn $\to 0$, we find that $Q_c^{ⓐ}, Q_c^{ⓑ} \to Q_c^{Ⓑ}$, while $Q_c^{ⓒ} \to Q_c^{Ⓔ}$. To see this, recall that invariant manifolds begin to intersect the collision sphere at these grazing bifurcations. This cannot happen for Kn $= 0$, where the radial mobilities vanish linearly in $\xi \equiv R - 2$ as $\xi \to 0$. In this limit, the grazing bifurcations must therefore coincide with bifurcations Ⓑ and Ⓔ, where a stable node appears or disappears at $R = 2$.

C. Collision rate

What are the consequences of these bifurcations for the collision rate? Figure 2(g) shows the steady-state collision rate $\mathscr{R}_\infty = \lim_{t \to \infty} \mathscr{R}_t$ for $a_1/a_2 = 0.9$ as a function of the nondimensional settling speed Q, for three different values of the Knudsen number: Kn $= 10^{-1}$, 10^{-2}, and 10^{-3}. Since the phase portraits in Fig. 2 suggest different behaviors for paths approaching from below and from above, the collision rate was computed separately for the two cases.

When the separatrices delineating collisions from no collisions are grazing trajectories, as in Fig. 2(a), the collision rate decreases as Kn decreases, as seen in Fig. 2(g) for $Q < Q_c^{ⓐ}$. The reason is that as the Kn number decreases, fewer trajectories approaching from large separations collide. However, Fig. 2(g) shows that the collision rate becomes independent of Kn for trajectories approaching from below, for small Kn, and for a certain range of nondimensional settling speeds Q (between bifurcations ⓐ and Ⓒ). This means that the collision rate does not vanish in this range for small Knudsen numbers.

The bifurcation analysis summarized above explains why the collision rate remains nonzero. The argument goes as follows. Between bifurcations Ⓐ and ⓐ there is a stable node at $R > 2$. In this regime, collision outcomes for trajectories from above are determined by a grazing trajectory, and so $\mathscr{R}_\infty$ depends on Kn. The fate of trajectories approaching from below is more subtle. Trajectories

approaching from below between the stable manifolds of IV and IV′ may either collide or asymptote to the stable node. Again, whether the trajectories collide or miss and approach the node depends on the Knudsen number. However, at bifurcation ⓩ, the invariant manifold connecting the stable node N to the saddle IV hits the collision sphere. As a consequence, all trajectories approaching from below between the stable manifolds of saddles IV and IV′ must collide. Since these fixed points and their stable manifolds are far from the collision sphere, for the Knudsen numbers considered, their location does not depend on Kn. This implies in turn that the collision rate is independent of Kn for trajectories approaching from below. This mechanism is analogous to that determining collisions of oppositely charged droplets settling in a quiescent fluid [6], where the separatrices are also formed by the stable manifolds of a saddle point of the collision dynamics. The former occurs when differential settling due to gravity and Coulomb attraction cancel. Thus the two bifurcations Ⓐ and ⓩ have important consequences for the collision rate: Ⓐ gives rise to the saddle IV, whose stable manifold determines the collision rate for trajectories approaching from below, for $Q > Q_c^{ⓩ}$.

The change in the mechanism determining the collision rate from a grazing trajectory for $Q < Q_c^{ⓩ}$ to an invariant manifold for $Q > Q_c^{ⓩ}$ leads to a sensitive dependence of the collision rate on Q near this bifurcation, seen as sharp peak near $Q = 5.67$ for the green curve in Fig. 2(g). The reason is that the collision rate jumps at $Q_c^{ⓩ}$ in the limit Kn → 0. Before the bifurcation, the collision rate tends to 0 as Kn → 0, but after the bifurcation the collision rate asymptotes to a nonzero Kn-independent limiting value.

Finally consider the small nonmonotonic bump in the collision rate for trajectories approaching from the upper half plane for very small Knudsen number Kn = 10^{-3}. Dhanasekaran *et al.* [11] pointed out that the bump is due to trajectories that encircle the collision sphere and collide from below. The Knudsen number needs to be small enough for this to occur, so that grazing separatrices, such as those in Fig. 2(c), can exist. At Kn = 10^{-3}, this gives a very small contribution to the collision rate. Nevertheless, this mechanism leads to a nonzero collision rate in the limit Kn → 0 when $Q_c^{Ⓑ} < Q < Q_c^{Ⓔ}$, for trajectories approaching from above.

D. Spatial clustering

The dynamics close to a saddle point can lead to an accumulation of trajectories—spatial clustering—if the stability exponents of the saddle point satisfy certain constraints. To find these conditions, we start from the steady-state continuity equation, obtained from Eq. (1) by setting $\frac{\partial P}{\partial t} = 0$. Now consider what happens close to the saddle point VI in Fig. 2(d). Its stable and unstable directions are $\hat{\mathbf{e}}_3$ and $\hat{\mathbf{e}}_1$, respectively. At the fixed point, $V = 0$. In its vicinity we linearize the velocity field $V_1 = \lambda_+ R_1$ and $V_3 = \lambda_- \delta R_3$, where λ_+ and λ_- are positive and negative stability exponents of the saddle and $\delta R_3 = R_3 - R_3^*$. The resulting steady-state continuity equation can then be solved using separation of variables. We find

$$P(R_1, \delta R_3) \sim |\delta R_3|^{-\lambda_+/\lambda_- - 1} \quad \text{as } R_1, \delta R_3 \to 0. \tag{6}$$

We conclude that P diverges algebraically as one approaches the unstable manifold in the vicinity of the fixed point, provided $0 > \lambda_+/\lambda_- > -1$.

Figure 3 shows results for $P(\mathbf{R})$ for $Q = 8$, $a_1/a_2 = 0.9$, and Kn = 10^{-3} obtained by numerically solving Eq. (1) using the method of characteristics. The saddle points V and VI are shown as encircled red crosses, just as in Fig. 2. The phase portrait for $Q = 8$ is similar to Fig. 2(d). For the saddle point VI, $\lambda_+/\lambda_- = -0.439$, and we observe regions of very large probability P that coincide precisely with its unstable manifolds. For the saddle point V, by contrast, $\lambda_+/\lambda_- = -1.23$. Since this ratio is smaller than −1, no clustering near its unstable manifold is expected. The large probabilities observed along the line $R_1 = 0$ are due to a different mechanism, explained next. The probability P diverges also very close to the collision sphere. This divergence, hard to see in Fig. 3 because it occurs so close to the collision sphere and because it is much weaker, was discussed in Refs. [11,32]. Since the radial relative velocity decays to zero as $V_R \sim (\log \log \frac{\text{Kn}}{R-2})^{-1}$ as $R \to 2$, the steady-state continuity equation implies that P diverges as $\sim 1/V_R$ in this limit.
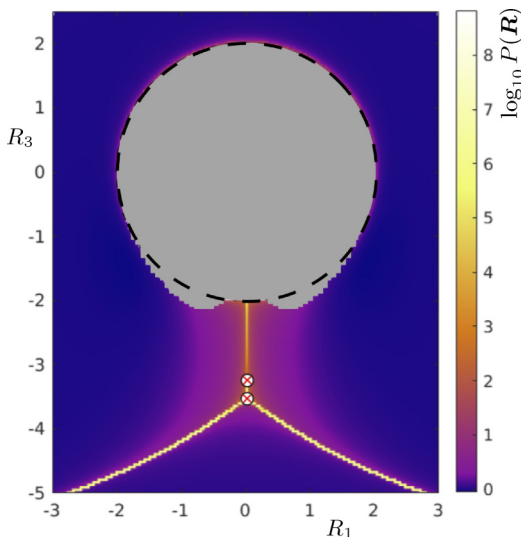
FIG. 3. Spatial clustering on invariant manifolds. Shown is the probability $P(\boldsymbol{R})$ for $Q = 8$, Kn $= 10^{-3}$ in the R_1-R_3 plane, color coded on a logarithmic scale. The probability diverges along manifolds of fixed point VI [see Fig. 2(d)]. The collision sphere is shown as a dashed circle. The encircled red crosses shows the location of the saddle points V and VI. The gray regions cannot be reached from $R = \infty$.

Near the saddle VI, the divergence is stronger. Consider the pair-correlation function $g(R)$. It is defined as the probability to find the two particles at separation R [9], $g(R) = \langle P(\boldsymbol{R}) \rangle_R$. Here the average is over the polar angle θ at a fixed separation R. Using Eq. (6), we find that $g(R)$ exhibits an algebraic divergence as $R \to R^*$.

IV. DISCUSSION

We concluded above that the collision rate for trajectories approaching from below becomes independent of Kn for small Kn between bifurcations Ⓐ and Ⓒ. Since Ⓐ is a grazing bifurcation, its location $Q_c^{Ⓐ}$ must depend on Kn. Equation (5) shows that $R^* - 2 \sim 10^{-8}$ when $Q \approx 6$, still very far from $Q_c^{Ⓑ} = 6.67$. In order to understand how Ⓐ depends on Kn, consider how the invariant manifold connecting IV and N approaches the node. Its eigenvalues have nonzero imaginary parts, which means that the manifold passes between the node and the collision sphere before it reaches the node. As a first rough estimate let us assume that this happens when $R^* - 2$ is of the order of Kn. Using this estimate and Eq. (5), we obtain $Q_c^{Ⓐ} \sim Q_c^{Ⓑ} + 20.49/\log$ Kn. This indicates that the Kn derivative of $Q_c^{Ⓐ}$ may diverge as Kn $\to 0$, implying that $Q_c^{Ⓐ}$ depends sensitively on the Knudsen number.

It is commonly stated that droplets cannot collide in the hydrodynamic approximation because it would take infinite time for them to touch [1,12–14], implying that the collision rate vanishes as Kn $\to 0$. However, we concluded here that this is correct only when the trajectory delineating collisions from no collision is a grazing trajectory, as in Fig. 2(a). In this case, the flux of colliding trajectories approaching from afar tends to zero because the grazing trajectories touch at $R_3 = \infty$ in the limit Kn $\to 0$, so the steady-state collision rate from above must vanish. However, when collisions are determined by the invariant manifolds of saddle points, as for the trajectories approaching from below in Fig. 2(b), the flux of approaching trajectories does not depend on Kn if the distance between the stable manifolds and the collision sphere is larger than Kn. The time these trajectories take to collide depends weakly on the Knudsen number, proportional to $\log(1/\text{Kn})$. So

the time it takes to collide grows as Kn → 0, but the steady-state collision rate remains finite in this limit, because the number density of droplets builds up as their dynamics slows down.

Our bifurcation analysis explains closed trajectories in relative dynamics, first reported by Batchelor and Green [15] and later by Zeichner and Schowalter [16] and Dhanasekaran *et al.* [32]. These closed trajectories arise because some trajectories starting close to the stable node N (or close to the stable nodes II, II′, or III, depending on the value of Q) start and end on the collision sphere. At larger values of Kn, there are more such closed trajectories, because some paths that grazed the collision sphere at small Kn collide instead. Zeichner and Schowalter [16] connected an observed decrease in collision rate to the appearance of such closed trajectories. Our results show, however, that is not the correct explanation, at least in the model considered here. The collision rate decreases between $Q_c^{\circledR}$ and $Q_c^{\copyright}$ because the collision rate for trajectories approaching from below decreases. Since the closed trajectories do not contribute to collision rate for trajectories approaching from below, they cannot explain the decrease of collision rate in this model. The correct explanation, outlined in the preceding section, is that the collision rate is determined by the stable invariant manifolds of the fixed points IV and IV′.

Only the bifurcations Ⓐ, Ⓒ, and Ⓓ are well explained by bifurcation theory for local equilibria in smooth dynamical systems, because they occur at $R^* > 2$ where the system is smooth. Bifurcations Ⓑ and Ⓔ occur at $R = 2$ where the system is not smooth: The radial derivative of the tangential mobility diverges. One consequence is the nonanalytic behavior described by Eq. (5), very different from the algebraic scaling observed for smooth systems [30] and also different from the behaviors found in piecewise smooth systems [18,19].

In our case, the collision dynamics stops at the boundary at $R = 2$ because we imposed that the droplets coalesce. Recent experiments [33] considered the collision dynamics of glass spheres in turbulence. Glass spheres may roll along the collision sphere at $R = 2$, leading to new bifurcations [34]. If the particles collided elastically instead, they could bounce. This might lead to interesting bifurcations similar to those seen in impacting systems [20]. We note also that Bragg *et al.* [33] observed pairs of spheres that stuck together. These could be the result of inelastic collisions, corresponding to a third qualitatively different collision outcome. All of the three cases mentioned above may result in new bifurcations and might even lead to chaotic dynamics [18].

In our analysis we considered only one value of the radius ratio, $a_1/a_2 = 0.9$. Because the mobility functions are not sensitive to changes of this ratio when it is close to unity [26], the bifurcation analysis should remain similar as the ratio becomes larger. The limit $a_1/a_2 \to 0$, by contrast, is expected to be quite different. In this case, Kn corrections to the tangential mobilities qualitatively change the dynamics [29]. How the phase-space portraits and the bifurcation diagrams change in this limit are open questions.

We assumed that the strain is aligned with gravity. Dhanasekaran *et al.* [11] studied numerically how the collision rate changes when the angle between strain and gravity changes. Their results indicate that the peak in the collision rate at $Q \approx 6$ is instead replaced by a minimum as the angle between strain and gravity changes. How are phase-space portraits affected and what are the corresponding changes to the bifurcation diagram? When strain and gravity are aligned, the dynamics is rotationally invariant. As a consequence, there is a continuous circle of fixed points [30], of which we considered only one pair, IV and IV′. For nonzero angles, this circle breaks up. Numerical simulations show that the qualitative conclusions regarding how the invariant manifolds determine collision outcomes remain similar for small but nonzero angles. An investigation for the future is to locate and characterize the new bifurcations that must occur as the angle is varied and to analyze their effect upon the collision rate.

The spatial clustering we described is very anisotropic because it occurs for large values of the nondimensional differential settling speed Q where gravity dominates. Another important point is that the probability diverges not only close to the particle, but also at separations of the order of a few droplet radii. As explained above, this is a consequence of the existence of saddle points in the relative dynamics. An open question is how misalignment between strain and gravity affects the spatial clustering. It is likely that an anisotropy persists if one averages over randomly

oriented strains, because gravity breaks up-down symmetry. However, the details remain to be worked out.

The results reported here concern very small, inertialess droplets. How do the phase portraits change when particle inertia is included? First, the full phase-space dynamics including velocities must be considered, as described in Ref. [6]. Second, particle inertia allows the particles to overshoot the saddle point IV in Fig. 3. This could reduce the spatial clustering. Third, while in the inertialess case the relative velocity at contact must vanish, inertia allows collisions at nonzero relative velocities [9], causing the collision rate to increase. An example is given by Bec *et al.* [35], who describe how particle inertia increases the collision rate of small particles colliding with a large one. Furthermore, for solid spheres, collisions at nonzero relative velocities could give rise to chaotic dynamics, similar to transitions to chaos observed in impacting systems [18].

Finally, our analysis considered steady flow. In time-dependent flow, such as turbulence, the bifurcation analysis becomes more difficult since one has to consider a driven dynamical system. In particular, it remains to be seen to what extent the spatial clustering is weakened when the flow becomes time dependent. We note that recent experimental studies [33,36] of colliding particle in turbulence show strong spatial clustering at small separations. Whether or not the clustering mechanism described above can offer an explanation of these observations depends on whether it survives averaging over different steady linear flows and to what extent it is weakened by stochastic driving in a time-dependent flow.

V. CONCLUSION

We investigated bifurcations in the collision dynamics of small droplets settling in a straining flow. We considered the case where the compressive direction of strain is aligned with gravity. We showed that the collision dynamics is not smooth because the radial derivatives of the mobility functions diverge on the collision sphere. As a consequence, we observed types of bifurcations that cannot occur in smooth dynamical systems where index theorems constrain the possible normal bifurcation forms. We found three different kinds of bifurcations: standard smooth bifurcations of equilibria, but also nonsmooth bifurcations of equilibria, as well as grazing bifurcations.

The grazing bifurcations determine the global phase portraits of the collision dynamics and explain that the collision rate approaches a nonzero constant for small Kn, for a range of nondimensional settling velocities. This is surprising, because it is commonly stated that droplets cannot collide in the hydrodynamic approximation [1,12–14], implying that the steady-state collision rate vanishes. Our results show that this argument is correct only when the trajectories separating colliding from noncolliding paths graze the collision sphere. This is the case for droplets with different radii settling in a quiescent fluid. However, when differential settling competes with a straining flow, we concluded here that these separatrices are, in a certain parameter range, formed by the stable manifolds of saddle points that are far from the collision sphere. In this case the steady-state collision rate becomes independent of the Knudsen number for small Kn.

Our analysis shows that saddle points may give rise to spatial clustering, causing trajectories to accumulate close to the saddle point in question, leading to a flux along the unstable manifold of the saddle. We demonstrated that this can result in an algebraic divergence of the pair-correlation function $g(R)$ at separations R of the order of several droplet radii. Since gravity breaks the up-down symmetry of the problem, the observed spatial clustering is highly anisotropic. When the compressive axis of the straining flow is aligned with gravity, there is a high probability of observing the larger sphere below the smaller one. This prediction may be tested experimentally by looking at snapshots of droplets in gravity-dominated straining flow.

Our results show that understanding smooth and nonsmooth bifurcations of the collision dynamics yields important insight into the physics of the collision process. In the future we therefore intend to perform this analysis for more general cases. The first step is to consider droplet radius ratios other than $a_1/a_2 = 0.9$. We expect that the results remain similar when the ratio is larger than

this value. However, when $a_1/a_2 \rightarrow 0$, the model considered here may fail because it neglects Kn corrections to the tangential mobilities which may become important in this limit.

Second, we intend to investigate the bifurcations when strain is not aligned with gravity.

Third, in order to describe droplet collisions in turbulence, we need to consider what happens when the flow is time dependent. In order to understand how the collision rate depends on Kn, the timescales at which stable manifolds of saddle points move have to be considered. Moreover, it is unclear to what extent spatial clustering survives in this case. If it does, it could be a mechanism for the extreme spatial clustering observed in recent experiments [33,36], which remains unexplained.

Fourth, particle inertia matters for larger droplets, because it allows them to detach from the flow [9]. The bifurcation analysis in this case is more challenging because it must be performed in phase space including separations and relative velocities.

Finally, in an earlier study [6], we analyzed the effect of electrical charges on the collision dynamics. Reference [6] did not account for the breakdown of the hydrodynamic approximation close to the collision sphere; therefore, we considered charges large enough that the relevant equilibria were far from the collision sphere. In this limit we found the phase portraits to be qualitatively different from those for neutral droplets. However, we do not know at what amount of charging this qualitative change happens. It might occur already for small charges of the order of typical charges observed in warm rain clouds [37]. This could have important implications for droplet collisions in rain clouds.

APPENDIX A: FIXED-POINT LOCATIONS OF I–III AND ANALYSIS OF BIFURCATION ⑩

Equation (3) can be expressed in radial and angular components of relative velocity $V_R \equiv \dot{R}$ and $V_\theta \equiv R\dot{\theta}$ as

$$V_R = -LQ \cos\theta + (A-1)\frac{R}{4}(1 + 3\cos 2\theta), \tag{A1a}$$

$$V_\theta = MQ \sin\theta + (1-B)\frac{3R}{4}\sin 2\theta. \tag{A1b}$$

Here L and M are the radial and tangential mobility functions for spheres due to sedimentation, while A and B are the radial and tangential mobility functions for spheres in shear flow [15,38].

Fixed points may be found by solving the equations $V_R = 0 = V_\theta$. The fixed points I, II, II′, and III lie on the collision sphere where $V_R = 0$. In order to find these fixed points, we must solve $V_\theta = 0$ at $R = 2$,

$$[M_0 Q - 3B_0 \cos\theta]\sin\theta = 0. \tag{A2}$$

Here B_0 and M_0 are the values of the tangential mobility functions upon contact. Equation (A2) has solutions $\theta^* = 0$ and π, corresponding to fixed points I and III, respectively. In addition, if $Q \leqslant 3B_0/M_0$ the equation has solutions $\theta^* = \pm \arccos \frac{M_0 Q}{3B_0}$. These correspond to fixed points II and II′. As Q increases from zero, the fixed points II and II′ move along the collision sphere until $Q_c^{\circledD} = 3B_0/M_0$ when they collide with III. This is bifurcation ⑩, a supercritical pitchfork bifurcation [30]. For $Q > Q_c^{\circledD}$, the equation $\cos\theta = \frac{M_0 Q}{3B_0}$ admits no real solutions.

APPENDIX B: FIXED-POINT LOCATION OF N AND ANALYSIS OF BIFURCATION ⑧

In order to compute the location $[R^*, \theta^*]$ of the node N, we solve $V_R = 0$ for the fixed-point angle,

$$\theta^* = \arccos\left(\frac{-4k - \sqrt{k^2 + 48}}{12}\right), \tag{B1a}$$

with

$$k = \frac{LQ}{(1-A)R^*}. \tag{B1b}$$

Inserting this expression for θ^* into $V_\theta = 0$, we obtain

$$3(1-B)\frac{R^*}{4}\sin 2\theta^* + MQ\sin\theta^* = 0. \tag{B2}$$

This is an implicit equation for R^* because the mobility functions as well as θ^* [Eq. (B1)] are functions of R^*. In general, this equation must be solved numerically; however, asymptotic solutions can be obtained when R^* is close to the collision sphere, using known asymptotic expansions for the mobilities for small $\xi \equiv R - 2$.

The radial mobility functions A and L depend upon the Knudsen number only through the functions Λ_{11}^{nc} and Λ_{21}^{nc} defined in Eqs. (4.2)–(4.6) in Ref. [11]. From their Eqs. (4.2) and (4.3), it follows that the ratio $L/(1-A)$ is independent of both Λ_{11}^{nc} and Λ_{21}^{nc}. Thus, the ratio $L/(1-A)$ does not depend upon the Knudsen number. For small ξ, this ratio approaches the constant [15,26,38]

$$\frac{L(\xi)}{1 - A(\xi)} \sim \frac{1}{C}. \tag{B3}$$

Equation (B3) allows us to approximate k in Eq. (B1b) as

$$k \sim \frac{Q}{C(2+\xi)} \quad \text{for } \xi \ll 1. \tag{B4}$$

The asymptotic expansions for the tangential mobilities in the limit $\xi \to 0$ read [26]

$$B, M \sim \frac{c_{B,M}^{(1)} \log^2\xi - c_{B,M}^{(2)}\log\xi + c_{B,M}^{(3)}}{\log^2\xi - e^{(1)}\log\xi + e^{(2)}}. \tag{B5}$$

The coefficients $c_{B,M}^{(i)}$ and $e^{(i)}$ depend only on the radius ratio a_1/a_2. While the coefficients $c_{B,M}^{(i)}$ in the numerator are different for the two mobility functions B and M, the coefficients $e^{(1)}$ and $e^{(2)}$ in the denominator are the same for these functions.

We now insert Eqs. (B5), (B4), and (B1a) into Eq. (B2), obtaining an equation for the fixed-point location valid for small ξ and $\eta \equiv -1/\log\xi$. In order to find its asymptotic solutions in the limit $\xi \to 0$, note that order-ξ terms are subleading to order-η terms. Ignoring the former, one obtains a quadratic equation in η. The solution yields η as a function of $\delta Q = Q_c^{⑧} - Q$,

$$\eta = f(\delta Q), \tag{B6a}$$

$$Q_c^{⑧} = B_0\sqrt{\frac{3C}{M_0(CM_0 - B_0)}}. \tag{B6b}$$

The function f has a zero at $Q = Q_c^{⑧}$, corresponding to the value of Q at which the node N touches the collision sphere. This corresponds to bifurcation ⑧. For $a_1/a_2 = 0.9$, we obtain $Q_c^{⑧} = 6.6759$, and the function f has the series expansion

$$f(\delta Q) = 0.0488\delta Q - 0.0255\delta Q^2 + 0.0147\delta Q^2 + \cdots \tag{B7}$$

in $\delta Q = Q_c^{\circledR} - Q$. Changing variables from η back to ξ, we arrive at

$$\xi = \exp[-1/f(\delta Q)]. \tag{B8}$$

Inserting $f(\delta Q) \approx 0.0488 \delta Q$ yields Eq. (5).

---

[1] H. R. Pruppacher and J. D. Klett, *Microphysics of Clouds and Precipitation* (Springer Netherlands, Dordrecht, 2010).

[2] A. Johansen, J. Blum, H. Tanaka, C. Ormel, M. Bizzaro, and H. Rickman, in *Protostars and Planets VI*, edited by H. Beuther, R. S. Klessen, C. P. Dullemond, and T. Henning (University of Arizona Press, Tucson, 2014).

[3] M. Wilkinson, B. Mehlig, and V. Uski, Stokes trapping and planet formation, Astrophys. J. Suppl. Ser. **176**, 484 (2008).

[4] K. Gustavsson and B. Mehlig, Relative velocities of inertial particles in turbulent aerosols, J. Turbul. **15**, 34 (2014).

[5] P. G. Saffman and J. S. Turner, On the collision of drops in turbulent clouds, J. Fluid Mech. **1**, 16 (1956).

[6] G. Magnusson, A. Dubey, R. Kearney, G. P. Bewley, and B. Mehlig, Collisions of micron-sized charged water droplets in still air, Phys. Rev. Fluids **7**, 043601 (2022).

[7] S. Kim and S. J. Karrila, *Microhydrodynamics: Principles and Selected Applications* (Butterworth-Heinemann, Boston, 1991).

[8] R. R. Sundararajakumar and D. L. Koch, Non-continuum lubrication flows between particles colliding in a gas, J. Fluid Mech. **313**, 283 (1996).

[9] K. Gustavsson and B. Mehlig, Statistical models for spatial patterns of heavy particles in turbulence, Adv. Phys. **65**, 1 (2016).

[10] J. D. Klett and M. H. Davis, Theoretical collision efficiencies of cloud droplets at small Reynolds numbers, J. Atmos. Sci. **30**, 107 (1973).

[11] J. Dhanasekaran, A. Roy, and D. L. Koch, Collision rate of bidisperse spheres settling in a compressional non-continuum gas flow, J. Fluid Mech. **910**, A10 (2021).

[12] L. M. Hocking, The effect of slip on the motion of a sphere close to a wall and of two adjacent spheres, J. Eng. Math. **7**, 207 (1973).

[13] R. H. Davis, The rate of coagulation of a dilute polydisperse system of sedimenting spheres, J. Fluid Mech. **145**, 179 (1984).

[14] A. Pumir and M. Wilkinson, Collisional aggregation due to turbulence, Annu. Rev. Condens. Matter Phys. **7**, 141 (2016).

[15] G. K. Batchelor and J. T. Green, The hydrodynamic interaction of two small freely-moving spheres in a linear flow field, J. Fluid Mech. **56**, 375 (1972).

[16] G. R. Zeichner and W. R. Schowalter, Use of trajectory analysis to study stability of colloidal dispersions in flow fields, AIChE J. **23**, 243 (1977).

[17] B. K. Brunk, D. L. Koch, and L. W. Lion, Turbulent coagulation of colloidal particles, J. Fluid Mech. **364**, 81 (1998).

[18] M. di Bernardo Laurea, A. R. Champneys, C. J. Budd, and P. Kowalczyk, *Piecewise-Smooth Dynamical Systems* (Springer, London, 2008).

[19] B. Brogliato, *Nonsmooth Mechanics* (Springer, Cham, 2016).

[20] S. Foale and S. R. Bishop, Bifurcations in impact oscillations, Nonlinear Dyn. **6**, 285 (1994).

[21] M. di Bernardo and S. J. Hogan, Discontinuity-induced bifurcations of piecewise smooth dynamical systems, Philos. Trans. Royal Soc. A **368**, 4915 (2010).

[22] G. Falkovich, A. Fouxon, and G. Stepanov, Acceleration of rain initiation by cloud turbulence, Nature (London) **419**, 151 (2002).

[23] M. Wilkinson and B. Mehlig, Caustics in turbulent aerosols, Europhys. Lett. **71**, 186 (2005).

[24] M. Wilkinson, B. Mehlig, and V. Bezuglyy, Caustic Activation of Rain Showers, Phys. Rev. Lett. **97**, 048501 (2006).

[25] K. Gustavsson, B. Mehlig, and M. Wilkinson, Collisions of particles advected in random flows, New J. Phys. **10**, 075014 (2008).

[26] D. J. Jeffrey and Y. Onishi, Calculation of the resistance and mobility functions for two unequal rigid spheres in low-Reynolds-number flow, J. Fluid Mech. **139**, 261 (1984).

[27] A. K. Townsend, Generating, from scratch, the near-field asymptotic forms of scalar resistance functions for two unequal rigid spheres in low-Reynolds-number flow, arXiv:1802.08226.

[28] H. Wang, A. Z. Zinchenko, and R. H. Davis, The collision rate of small drops in linear flow fields, J. Fluid Mech. **265**, 161 (1994).

[29] M. L. S. How, D. L. Koch, and L. R. Collins, Non-continuum tangential lubrication gas flow between two spheres, J. Fluid Mech. **920**, A2 (2021).

[30] S. H. Strogatz, *Nonlinear Dynamics and Chaos: With Applications to Physics, Biology, Chemistry and Engineering* (Westview, Boulder, 2000).

[31] E. Ott, *Chaos in Dynamical Systems*, 2nd ed. (Cambridge University Press, Cambridge, 2002).

[32] J. Dhanasekaran, A. Roy, and D. L. Koch, Collision rate of bidisperse, hydrodynamically interacting spheres settling in a turbulent flow, J. Fluid Mech. **912**, A5 (2021).

[33] A. D. Bragg, A. L. Hammond, R. Dhariwal, and H. Meng, Hydrodynamic interactions and extreme particle clustering in turbulence, J. Fluid Mech. **933**, A31 (2022).

[34] M. R. Jeffrey and S. J. Hogan, The geometry of generic sliding bifurcations, SIAM Rev. **53**, 505 (2011).

[35] J. Bec, C. Siewert, and R. Vallee, Effect of gravitational settling on the collisions of small inertial particles with a sphere, arXiv:2009.03154.

[36] M. A. Yavuz, R. P. J. Kunnen, G. J. F. van Heijst, and H. J. H. Clercx, Extreme Small-Scale Clustering of Droplets in Turbulence Driven by Hydrodynamic Interactions, Phys. Rev. Lett. **120**, 244504 (2018).

[37] T. Takahashi, Measurement of electric charge of cloud droplets, drizzle, and raindrops, Rev. Geophys. **11**, 903 (1973).

[38] G. K. Batchelor, Sedimentation in a dilute polydisperse system of interacting spheres. Part 1. General Theory, J. Fluid Mech. **119**, 379 (1982).